Electrochemical hydrogen permeation in wrought and electron beam melted Ti-6Al-4V alloys

May Hayoun [a], Noam Eliaz [a,*], Nissim U. Navi [b], Noa Lulu-Bitton [a,b], Pini Shekhter [c], Eyal Sabatani [a,b,**]

[a] Department of Materials Science and Engineering, Tel-Aviv University, Ramat Aviv, Tel Aviv 6997801, Israel
[b] Nuclear Research Center Negev (NRCN), P.O. Box 9001, Beer Sheva 84910, Israel
[c] Center for Nanoscience and Nanotechnology, Tel-Aviv University, Ramat Aviv, Tel Aviv 6997801, Israel

ABSTRACT

Ti-6Al-4V is one of the most widely used titanium alloys. However, it is susceptible to hydrogen embrittlement, e. g. due to hydride formation. Hydrogen permeability through Ti-based alloys is affected by the rapid formation of hydride or oxide surface layers as well as by trapping in the bulk alloy. Here, we analyze and compare the electrochemical hydrogen permeation (EHP) through wrought and electron beam melted (EBM) Ti-6Al-4V alloys. Hydrogen diffusion coefficients are calculated from the permeation current transients. The effective diffusion coefficient of hydrogen in the wrought alloy is found to be an order of magnitude higher than in the AM'ed alloy. The different microstructures of the wrought and EBM alloys are found to play an important role in hydrogen distribution and phase transformation in the alloy. In the EBM alloy, hydrogen is distributed more uniformly and, consequently, more pronounce phase transformations occur, eventually leading to brittle cracking. In the wrought alloy, on the other hand, hydrogen is distributed unevenly in the bulk of the membrane, forming hydride clusters, most probably at α/β interphase boundaries. These findings suggest that the EBM Ti-6Al-4V alloy is more susceptible to HE than its wrought counterpart.

1. Introduction

Titanium and its alloys are important structural materials that are widely used in the aerospace, automobile, marine and nuclear industries, as well as in biomedical applications [1–5]. The microstructure of Ti-based alloys is significantly affected by their manufacturing process, addition of alloying elements, or complementary thermomechanical processing [5,6]. Titanium alloys are usually categorized according to their microstructure at room temperature as near-α (hcp), metastable-β, near-β, or stable-β (bcc), or α + β (dual hcp + bcc) alloys [5–7]. Ti-6Al-4V is the most common titanium alloy, representing almost 50% of the market share of titanium products [2,6]. It is an α + β alloy, and its microstructure and β-content are affected by the thermal conditions during processing or thermal post-treatment.

Electron beam melting (EBM) is a common powder-bed fusion additive manufacturing (PBF-AM) process. The potential use of EBM for manufacturing of parts from titanium alloys, including Ti-6Al-4V, for aerospace and biomedical implant applications, has been studied [8,9]. The microstructure of EBM Ti-6Al-4V is complex due to the distinct thermal conditioning during manufacturing, in particular the rapid solidification and the repeated thermal cycles as successive layers of molten metal are being deposited [10,11]. EBM Ti-6Al-4V has a microstructure consisting of major α-phase and minor β-phase. The lamellar α + β microstructure is known as Widmanstätten (or, basket-weave) [12,13].

Titanium and its alloys are prone to hydrogen embrittlement (HE), mainly due to the formation of brittle hydrides and their cracking [14–18]. The exposure to either gaseous or electrochemical hydrogen can occur during primary or secondary manufacturing processes (e.g. AM, welding, machining), post-treatments (e.g. heat treatments or electroplating), or during storage, service, or maintenance. The diffusivity and solubility of hydrogen in the β-phase are significantly higher than in the α-phase [19–25]. The higher solubility and higher diffusion coefficient in the β-phase result from the relative abundance of

---

interstitial sites in its crystal structure: 12 tetrahedral and 6 octahedral interstitial sites in the β-phase, compared with only 4 and 2 sites, respectively, in the α-phase [21]. Hydrogen at low concentrations in titanium alloys forms α_H and β_H solid solutions, while at higher concentrations – γ, δ, and ε hydride phases are formed [17,21,26].

In Ti-6Al-4V, hydrogen diffusion occurs favorably within the β-phase lattice; subsequently, hydrogen reacts with the α-phase at the α/β interphase boundaries [27,28]. At hydrogen concentrations exceeding the solubility limit, brittle titanium hydride phases start to precipitate at the α/β interphase boundaries [18,21]. The presence of hydrogen in solid solution in either the α or β phase increases the microstrain in the alloy due to lattice expansions [21,27,29]. Stress gradients direct hydrogen diffusion and enhance further hydride formation and initiation of cracks, mainly along the α/β interphase boundaries or in the α phase, depending on the prior microstructure of the alloy [27].

Defects, such as dislocations, grain boundaries, pores and interphase boundaries can affect the diffusivity and solubility of hydrogen in the alloy, as they provide potential trapping sites for hydrogen [30,31]. In dual phase α + β titanium alloys, the most prominent trapping sites are the α/β interphase boundaries [27]. Traps are known to affect the distribution of hydrogen in the alloy [32]. Distinction between reversible and irreversible traps is made [32,33]. When the metal is preloaded with hydrogen, reversible sites can serve as a source for hydrogen and may facilitate its diffusion towards potential crack nucleation sites, thereby increasing the risk of cracking [32].

AM'ed Ti-6Al-4V alloy, with its unique microstructure, is expected to exhibit complex hydrogen behavior [14,28,34–36]. First, the fine lamellar structure provides ample of α/β boundaries. The fine microstructure also provides a continuous network of β-phase grains, which facilitate hydrogen transport through the bulk of the alloy [28,35]. In addition, residual thermal stresses, which arise from the AM process, may also affect the behavior of hydrogen in the alloy.

Electrochemical hydrogen permeation (EHP) tests have been used extensively to study the diffusivity and solubility of hydrogen in metals and alloys. These tests typically employ the Devanathan-Stachurski (DS) electrochemical cell [37–41], which comprises of two separate cells, one serving as the charging cell (with catholyte), and the other as the detection cell (with anolyte), with the specimen membrane separating the two. The permeation current is directly proportional to the flux of hydrogen at the exit surface. Hydrogen diffusivity can thus be calculated from the sigmoidal shaped permeation transient, assuming that mass transport of hydrogen through the membrane is diffusion limited [39–42]. The subsurface hydrogen concentration at the entry side can also be calculated from the transient, using Fick's first low of diffusion and assuming that a linear hydrogen concentration gradient is built across the membrane at steady state [39–41].

We could find only two articles that reported the results of EHP in Ti-6Al-4V [43,44], and no article that reported EHP in AM'ed Ti-6Al-4 V. Estupiñan et al. [43] compared the EHP in three γ-TiAl intermetallic compounds to that in wrought Ti-6Al-4V. The tests were conducted in 0.1 N NaOH (pH 12.6) at 298 K. The apparent diffusion coefficient (possibly affected by hydride formation) in the Ti-6Al-4V alloy was 3.26 $\times 10^{-6}$ cm^2/s. This value was twice that in a fully lamellar alloy. It was claimed that the microstructure had only a minor effect on the diffusivity because hydrogen diffusion occurred primarily via lattice diffusion paths. Although it was assumed in Ref. [43] that hydrides were formed on the entry surface, no supporting information was provided, and the effects of hydrogen on the microstructure of the alloy membranes was not provided either. Huang et al. [44] showed that laser peening could reduce the apparent hydrogen diffusivity in wrought Ti-6Al-4V. The authors attributed this improvement to an increased internal stress level in the material, which hindered hydrogen ingress. Their EHP tests were conducted using a 0.1 M NaOH anolyte, a 1 M H$_2$SO$_4$ catholyte to which Na$_4$P$_2$O$_7$·10 H$_2$O was added as a surface poisoner to increase hydrogen absorption in the membrane. Nickel coating was applied on the exit (anodic) side of the membrane to reduce

background corrosion currents. Before laser peening, the apparent hydrogen diffusivity was 6.26 $\times 10^{-7}$ cm^2/s. While microhardness measurements on the surface of the samples revealed increase in hardness following hydrogenation, which could be related to hydride formation, no supporting microstructural and chemical characterization was presented. Reproducing the results in Refs. [43,44] is challenging because the experimental description therein is incomplete. There is also a lack of information about post-permeation sample examination, leaving gaps in our understanding of how the membranes were affected by the EHP test. It should be noted that the breakthrough times (t_b, found by extrapolating the linear portion of the initial rising current transient to zero flux) reported in Refs. [43,44] were very short (less than 46 s and 300 s, respectively), and that the reported diffusion coefficients were higher than expected. For comparison, Devanathan and Stachurski reported t_b = 433 s and D_{eff} = 1.10 $\times 10^{-7}$ cm^2/s for Pd [39], which is known for the high permeability of hydrogen in it. Moreover, the diffusion coefficients reported in Refs. [43,44] are higher than those reported for either the α-phase or β-phase [14,17,21,24,25,45]. For a duplex α + β alloy one could expect the D_{eff} value to fall between those of in the α and β phases, which was not the case in Refs. [43,44].

Here, the diffusivity of hydrogen in AM'ed Ti-6Al-4V is measured for the first time by the EHP technique, in comparison to wrought Ti-6Al-4V. Proper experimental conditions for reliable EHP data are identified. Complementary microstructural characterization is provided to better understand the effect of microstructure on EHP in both alloys. While the EBM alloy has a fine Widmanstätten lamellar structure, the wrought alloy has an equiaxed grain structure. The effect of β-phase content can be ignored because it is similar (4–5%) in both alloys.

2. Materials and methods

2.1. Sample preparation

Wrought Ti-6Al-4V Grade 23 (Extra Low Interstitial) rod, 11 mm in diameter, was produced by Dynamet, Inc. (Washington, PA, vendor Barmil, Petach Tikva, Israel). Transverse disk-shape samples (i.e., perpendicular to the extrusion direction) were cut by electric discharge machining (EDM). Rods of EBM Ti-6Al-4V alloy, 13 mm in diameter, were manufactured at the AM Center of Rotem Industries Ltd. (Mishor Yamin, Israel), using an Arcam Q20 Plus system and a Grade 5 spherical powder with a size range of 45–106 μm. Printing parameters were set to accelerating voltage of 60 kV, beam current of 28 mA, speed function of 32 (~2400 mm/s base beam speed), and layer thickness of 90 μm. The temperature was maintained in the range of 750–850 °C. A chamber pressure of 4 $\times 10^{-3}$ mbar was regulated utilizing a helium leak valve. Disk-shape samples were cut from the rod by EDM in the traverse direction, i.e. with the cut plane perpendicular to the build direction.

2.2. Electrochemical hydrogen permeation experiments

The diffusion coefficients were determined by EHP experiments, using a homemade DS double cell and adhering to the ASTM G148–97 (2018) guidelines [40]. At least three samples of each alloy type were tested. Pre-cut disk samples were ground on both sides with 1200 P SiC paper and mechanically polished down to 1 μm, using diamond pastes. The polished samples were ultrasonically cleaned in ethanol for 15 min. Their final thickness was 90–100 μm, thus the samples' final radius-to-thickness ratio was ca. 40, higher than the minimal value of 10 recommended in [40]. We also found that thicker samples resulted in impractically long permeation experiments.

In order to overcome the challenge of measuring hydrogen permeation currents in Ti-based alloys, the native titanium oxide layer on the surface of the membranes, which acts as a diffusion barrier to hydrogen, was first removed carefully (see procedure bellow), and immediately afterwards a protective coating was applied to prevent reoxidation. Nickel was used as a protective coating on the exit side in Refs. [44,45]

to avoid dissolution or passivation of the specimen surface [44] and as a catalyst of the hydrogen ion oxidation reaction [45]. However, palladium [46] is a better hydrogenation catalyst than nickel. The catalyst in the case of nickel is actually NiO [47], and it could be difficult to stabilize the desired oxidation state of nickel in the oxide.

The samples were immersed for 5 s at room temperature in an activation solution comprised of 2.5 N HNO_3 and 20 g/L NaF (a mild variant of Kroll's reagent). Subsequently, they were rinsed in distilled water and ethanol. Then, the samples were stored in a customized vacuum cell, which was opened only in a glove box under nitrogen atmosphere (water content $\leq$ 0.6 ppm, oxygen content $\leq$ 0.6 ppm) before being inserted into the etching and coating chamber. To eliminate any residual titanium oxide, the samples underwent surface treatment by argon ion-beam milling in the deposition chamber of an E-beam evaporator VST system (Petah Tikva, Israel) at the Center for Nanoscience and Nano-technology of the Hebrew University of Jerusalem. The samples were positioned on a rotating sample holder, which was cooled down to 10 °C. Immediately before Pd deposition, the samples' surface was argon ion-beam milled for 2 min under 3.2 sccm argon-gas flow, 2 A emission current, 2 A discharge current, and 150 V discharge voltage. The chamber's vacuum pressure was kept at 1×10^{-6} torr throughout the milling and deposition process. In order to protect the samples against oxidation, minimize the background current, and facilitate hydrogen absorption, the membranes were coated with a thin palladium film [36, 37,39,40]. This deposition was done by thermal evaporation, using an E-beam VST evaporator (Petah Tikva, Israel). 20 $\pm$ 1 nm Pd film was applied on each side of the alloy membrane at a deposition rate of 0.7 Å/s, using 99.99% palladium target (Materion, OH, USA). After deposition, the samples were stored in a desiccator until they were assembled in the EHP cell. It should be noted that ASTM G148 recommends covering only the exit (anodic) side of the membrane, to avoid background current caused by oxidation of the titanium surface. However, we found out that a significant titanium oxide layer formed on the entry (charging) side too, inhibiting the absorption of hydrogen in the membrane. Hence, it was decided to apply the Pd coating on both sides of the membrane.

The EHP experimental setup was described in detail before [36]. In brief, the sample membranes were assembled between the two compartments of a homemade DS double cell. The circular area on each side of the membrane exposed to the electrolyte was 0.5 cm^2. 0.1 M NaOH solution was used, both as catholyte and as anolyte. Deionized water was used to prepare all aqueous solutions as well as for rinsing. The potential and current were regulated using a computer-operated multi-channel BioLogic SP-300 Potentiostat/Galvanostat, which also recorded the resulting anodic current. During hydrogen charging, the entry (cathodic) side of the membrane was galvanostatically polarized at a constant current density of -2 mA/cm^2. During decay, the hydrogenation current density was lowered to a nearly zero value of -2 nA/cm^2. At the exit side, the membrane was held at a constant potential of $+ 0.15$ V vs. Hg/HgO/0.1 M NaOH reference electrode (–0.076 V vs. SCE), to ensure complete oxidation of hydrogen coming out at the exit side. All experiments were conducted at room temperature (around 25 °C) with continuous argon gas (99.999% pure) purging over the electrolyte solution in both compartments. Pt mesh served as a counter electrode in each cell. The reliability of the system and validity of the results were tested by comparing the results obtained with a Pd-0.3 wt% Pt membrane specimen to reported values [38,48].

Various electrolytes (both anolytes and catholytes) were evaluated when optimizing the experimental procedure. These included 0.1 M NaOH, 0.2 M NaOH, 0.1 M NaOH with surface poisoner (1-Ethyl-3-methylimidazolium thiocyanate); 0.5 M H_2SO_4, 0.05 M H_2SO_4 with surface poisoner (5 g/L NaSCN); H_3PO_4:glycerin mixture (1:2 ratio by volume). It was eventually concluded that 0.1 M NaOH without surface poisoner gave the best results, serving both as anolyte and as catholyte. Prior to the addition of the solution to the cells, it was vigorously purged with argon gas for at least an hour, to eliminate any traces of oxygen.

First, the electrolyte solution was introduced to the anodic cell, and a constant potential was applied on the exit side of the membrane. The catholyte was added to the cathodic cell only after the background oxidation current reached a value lower than 0.01 μA, ensuring complete "degassing" of residual hydrogen from the membrane, as well as that the "noise" signal during EHP experiments is significantly lower than the permeation current, thus achieving sufficiently high sensitivity.

Cyclic voltammetry (CV) was used to verify the effect of Pd coating and identify the oxidation and reduction regimes for wrought Ti-6Al-4V in 0.1 M NaOH at room temperature. The CV curves were acquired at a sweep rate of 20 mV/s, moving from positive to negative potential (forward scan), and then from negative to positive potential (reverse scan) to mimic the hydrogen exit (anodic) side. To mimic the hydrogen entry (cathodic) side, the opposite sequence of potential sweeps were run.

The diffusion coefficient was calculated from the experimental permeation transients by two different approaches: (1) fitting the permeation transient to an approximate solution of Fick's second law, and (2) from the time-to-breakthrough (t_b) [49]. In each of these methods, it is assumed that the concentration of subsurface hydrogen on the entry side is maintained constant, while at the exit side hydrogen is immediately oxidized and is kept at a near-zero concentration [39,40]. Assuming that the mass transport of hydrogen through the metal is diffusion controlled, the hydrogen diffusion coefficient can be calculated using the one-dimensional form of Fick's laws [50]:

$$\text{Fick's first law}: \quad j = -FD\frac{dc_H}{dx} \tag{1}$$

$$\text{Fick's second law}: \quad \frac{\partial c_H}{\partial t} = D\frac{\partial^2 c_H}{\partial x^2} \tag{2}$$

where t is time, D is the diffusion coefficient (cm^2/s), $c_H(x,t)$ is the lattice concentration of hydrogen as a function of position and time (mol/cm^3), j is the diffusional current density (A/cm^2), x is the position across the membrane, and F is the Faraday constant (96485 C/mol).

In order to solve these equations, it is necessary to define the boundary conditions in the experiment. In a typical EHP test, the initial and boundary conditions are as follows:

$$\begin{aligned} t = 0: \quad & c = 0 \text{ for } 0 \leq x \leq L \\ t > 0: \quad & c_{x=0} = c_H^0, c_{x=L} = 0 \end{aligned} \tag{3}$$

where L is the membrane thickness (cm) and c_H^0 is the subsurface concentration of atomic hydrogen at the entry side (assuming that subsurface hydrogen atoms reside in reversible traps only). The solution for Fick's second law is given by a Laplace series [50]:

$$\frac{J(t)}{J_{ss}} = \frac{2L}{\sqrt{\pi Dt}} \sum_{n=0}^{\infty} \exp\left(-\frac{(2n+1)^2 L^2}{4Dt}\right) \tag{4}$$

where $J_{ss} = j_{ss}/F$ is the atomic hydrogen permeation flux at steady state (mol/(s·cm^2)).

One can replace L^2/Dt with dimensionless time τ, defined by:

$$\tau = \frac{Dt}{L^2} \tag{5}$$

To determine the diffusion coefficient and to confirm the validity of Fick's second law, the experimental hydrogen permeation transient is fitted to the Laplace series, which represents the analytical solution of Fick's second law. An experimental transient steeper than that predicted by Fick's second law may indicate a significant presence of traps. On the other hand, if the permeation transient exhibits a less steep profile than that predicted by Fick's second law, it is frequently an indication of unsteady surface conditions [40].

The breakthrough time method is used herein to calculate the effective diffusion coefficient. The relationship between the break-

through time and the effective diffusion coefficient is [39]:

$$D_{eff} = \frac{L^2}{15.3\, t_b} \tag{6}$$

2.3. 2.3. Microstructural and chemical characterization

Scanning electron microscopy (SEM) images were acquired using a Quanta 200 FEG ESEM (FEI, MA, USA) microscope, equipped with an Oxford X-Max silicon drift detector (SDD, Abington, UK) for energy-dispersive X-ray spectroscopy (EDS). Samples for SEM analysis were cut either longitudinally or transversely, were mounted in an EpoFix resin, mechanically ground and polished down to 1 μm with diamond paste, and were finally subjected to chemical etching in Kroll's reagent (10 mL HF, 30 mL HNO₃, 50 mL H₂O) for 7–10 s. X-ray diffraction (XRD) analysis was conducted at room temperature using a D8 ADVANCE diffractometer with a Bragg-Brentano geometry (Bruker AXS, Madison, WI, USA) and a Cu-Kα radiation source ($\lambda = 1.5418$ Å). A linear position-sensitive device (PSD) detector (LYNXEYE XE-T) with an opening of 2.94° was used. Data points were acquired at increments of 0.02° and an acquisition time of 0.25 s. The scanning range was set to $2\theta = 10\text{–}90°$, but in this report, information is presented within the range of 34–43° to highlight the major changes. The lattice parameters and phase content were calculated by Rietveld refinement, using TOPAS software (version 5, Bruker AXS, Madison, WI, USA). The fitting was carried out for zero-error, lattice parameters, and phase composition. To ensure accuracy, the peak positions and peak shapes were calibrated using NIST Si 640e and LaB6 660c standard reference materials, respectively. Peaks were fitted using a TCHZ function type, and the asymmetry parameters (U, W, V) were determined using LaB6 660c and were fixed to account for instrumental contributions to peak shape.

Time-of-flight secondary ion mass spectrometry (ToF-SIMS) [22,28, 51,52] was used to map total hydrogen and titanium hydrides and establish their local intensity correlations with microstructural features in the alloys. The measurements included local hydrogen line scan profiles along the longitudinal cross-section. A Physical Electronics TRIFT II system (PHI, USA) was used at 15 keV and 600 pA Ga⁺ ion beam for mass spectra, and 25 keV and 60 pA Ga⁺ ion beam for imaging. Signals obtained for negative secondary ions (H⁻, TiH_x^- ($x = 1\text{–}5$) and Ti⁻) were used to map the fine-polished longitudinal cross-sections of the membranes after EHP tests. Prior to analysis, 2 keV, 150 nA Cs⁺ ion beam was employed to sputter-clean the surface [53]. To avoid suboptimal vacuum conditions as a result of epoxy mounting, a custom-made stainless steel sample holder was used for mounting. The chamber was maintained at a high vacuum of approximately 5×10^{-10} torr. Ion images were acquired from a freshly sputtered surface using Cs⁺ sputtering, which enhances the yield of negative ions, especially H⁻. To prevent recontamination that could lead to higher hydrogen reading in subsequent images, a short stage of image collection with the Ga⁺ analytical gun was followed by a brief sputter stage, with the Cs⁺ sputter gun lasting two seconds. The accuracy of the SIMS analysis was in the order of several percent. It should be noted that absolute concentrations cannot be reported herein in the absence of calibration standards.

Auger electron spectroscopy (AES) measurements were performed on the membrane cross-section, using a Thermo Scientific™ ESCALAB QXi instrument (MA, USA) at high-vacuum conditions, with a base pressure of 10^{-10} mbar, primary beam energy of 5 kV, beam diameter of approximately 50 nm (which is equivalent to 200 nm spatial resolution), and a constant retard ratio of 40. High-resolution spectra were acquired at pass energy of 10 eV and 0.5 eV intervals. Prior to measurement, the surface of the cross-section was sputter-cleaned in-situ, using 4 kV argon gun with a 3×3 mm² raster size for 600 s, to remove residual oxide and random contaminations. The Avantage software package (version 6, Thermo Scientific™) was used for data analysis. Titanium hydride (TiH₂) content was calculated from the differential spectrum through peak superposition analysis of the AES spectra. The peak ratio of the relevant peaks in each spectrum was compared with the peak ratios obtained from reference spectra corresponding to non-hydrogenated Ti-6Al-4V alloys and to TiH₂ powder (>98%, Merck, MA, USA). Comparison of peak ratios using the lever rule gives normalized peak ratio values in the range of 0–100% TiH₂ content, representing the degree of hydrogenation. The advantage of relying on the normalized ratios rather than a single peak value is that even in non-ideal situations, the proportions between two peaks will remain consistent. The calculation procedure of TiH₂ content was developed during this study and is presented in more detail below.

3. Results

3.1. Determination of appropriate experimental conditions for EHP by cyclic voltammetry (CV)

Typical cyclic voltammograms of both uncoated (black line) and Pd-coated (blue line) samples are shown in Fig. 1. Scanning in the negative potential direction (forward scan) results in water reduction and hydrogen evolution, whereas in the backward scan (in the positive potential direction) – hydrogen oxidation followed by either titanium oxidation (uncoated sample) or Pd oxidation (coated sample) are evident. In the case of the uncoated sample, water reduction and hydrogen evolution start during forward scan at ca. −1.0 V; at −1.65 V, the current density reaches −0.3 mA/cm². In the case of the Pd-coated sample, on the other hand, the reduction peak started at ca. −0.8 V, and the cathodic current density reached −1.6 mA/cm² at −1.2 V. In the reverse scan (in the positive potential direction), a significant current peak is evident at −0.62 V. This peak can be attributed to hydrogen oxidation. Once all the surface-adsorbed hydrogen is oxidized, the current drops and a plateau is reached. At a more positive potential (ca. −0.1 V), the current slightly increases due to Pd oxidation. In the opposite direction, a current peak likely related to palladium oxide reduction [54] is evident. In a second oxidation sweep (not shown herein), the hydrogen oxidation peak was not apparent, indicating that all surface-adsorbed hydrogen had been oxidized earlier, or simply desorbed into the solution. In the case of the uncoated sample, when the sequence of forward/backward scans was repeated (not shown herein), the current density decayed and remained constant at nearly zero due to the growth of a stable passive titanium oxide layer. In the case of the Pd-coated sample, on the other hand, the shape of the CV curve did not change during repeated oxidation sweeps, indicating that the electrode remained active, and that the formation of a surface barrier such as a titanium oxide layer [55] was avoided. Based on the preliminary CV
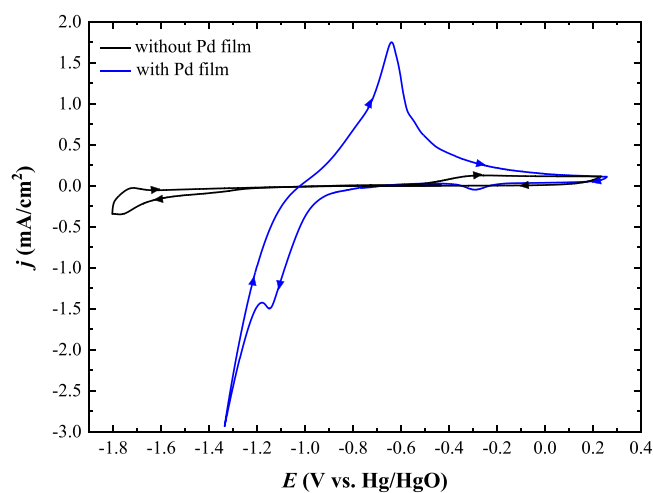

Fig. 1. Cyclic voltammograms of wrought Ti-6Al-4V membranes either uncoated (black curve) or coated (blue curve) with Pd. Arrows mark the sweep direction.

experiments, the current density at the entry (cathodic) side was set at -2 mA/cm^2 in the EHP experiments, while the anodic potential at the exit side was set at $+0.15$ mV, high enough to ensure that the reaction was diffusion controlled, and not charge transfer controlled.

3.2. EHP characteristics of wrought and EBM Ti-6Al-4V alloys

Fig. 2a displays a representative sequence of two charge/discharge cycles for wrought Ti-6Al-4V. During the first charging step, a current rise appears after an incubation period, and the breakthrough time, t_b, can be determined. The current continues to rise until it reaches an unstable plateau ("steady state"). Once the charging current is stopped, the permeation current decays. In the second charge/discharge cycle, a clear current transient is also evident, albeit with significantly different characteristics: the peak current is higher, and current spikes do not allow determination of a steady-state current. When the charging current is interrupted, a sharp decrease in the permeation current is observed. Noisy transients indicate that the membrane is undergoing structural (or compositional) changes during the permeation test [40], such as void or crack formation, either at the surface or in the bulk of the membrane. The breakthrough time in the second rise transient was longer than in the first transient (1036.2 min vs. 767.9 min, respectively), opposite to the typical behavior. Typically, since only reversible traps play a role in the second cycle, shorter breakthrough time is

expected in the second cycle [40,56]. Thus, it could be concluded that irreversible traps or surface barriers (e.g. hydride layer) affect the second rise transient and hinder hydrogen transport through the membrane.

After the EHP tests, both the entry and exit sides of the membranes were carefully inspected under a stereomicroscope. In the case of the wrought alloy, the color of the entry side of the membranes changed to yellow-blueish, while that of the exit side was matte gray. Additionally, deformation and loss of planarity was observed, the entry side exhibiting a convex shape (i.e. bent outwards) and small bumps, mostly at the center. Membranes made of EBM Ti-6Al-4V alloy showed similar color changes. But, cracks were also apparent on both sides. Such penetrating cracks could serve as short-circuit paths for hydrogen diffusion and change the shape of the permeation curves. Based on the aforementioned findings, it was decided to use only the first rise transient for the calculation of the effective hydrogen diffusion coefficient and the undersurface traps concentration.

Fig. 2b,c display representative current transients for wrought and EBM Ti-6Al-4V alloys, respectively. Significant difference is evident; the breakthrough time is significantly longer for the EBM alloy than for the wrought alloy, suggesting that hydrogen diffusion in former is slower. Next, the permeation current increases rapidly to 2 mA/cm^2, the same value as the applied charging current. It is thus suspected that hydrogen leaks through the membrane and is directly electro-oxidized at the exit side. We observed a similar behavior when the as-fabricated membrane contained penetrating pores; in that case, no incubation time was observed and the current rise was instantaneous. Nevertheless, in Fig. 2c incubation time is apparent, and the current rises gradually, indicating that leaks started playing a role only at a later stage of the test, after the sample was already significantly loaded with hydrogen. Hence, the marking of t_b in Fig. 2c seems to be legitimate.

To confirm that the permeation transient obtained for wrought Ti-6Al-4V followed Fick's second law, a normalized form ($j(t)/j_{ss}$ vs. τ) of the first rise transient was drawn and compared to the theoretical transient, Eq. (4), see Fig. 2d. According to ASTM G148–97 [40], substituting $n = 0$–6 in Eq. (4) yields sufficient accuracy. Since the "steady state" current was unstable and noisy, j_{ss} was also determined from the best fit; D_{eff} values were varied in Eq. (4) until the best fit was obtained. It is evident from Fig. 2d that this procedure yielded a reasonable fit of the experimental data, allowing derivation of D_{eff} for the wrought alloy. A similar fitting procedure was not applied to the EBM alloy because no plateau current could be identified in this case. Table 1 tabulates the D_{eff} determined based on the experimental breakthrough time, as well as those derived from the Laplace series fit (for the wrought alloy). In the case of the wrought alloy, similar D_{eff} values are obtained by both methods, indicating that hydrogen permeation through this membrane is diffusion controlled. D_{eff} in the EBM alloy is about an order of magnitude smaller than in the wrought alloy. Compared to the values reported for wrought Ti-6Al-4V in Refs. [43,44], the D_{eff} values in this study are considerably lower.

Because the experimental transient is steeper than that predicted by Fick's second law, it can be claimed that traps and/or surface films have
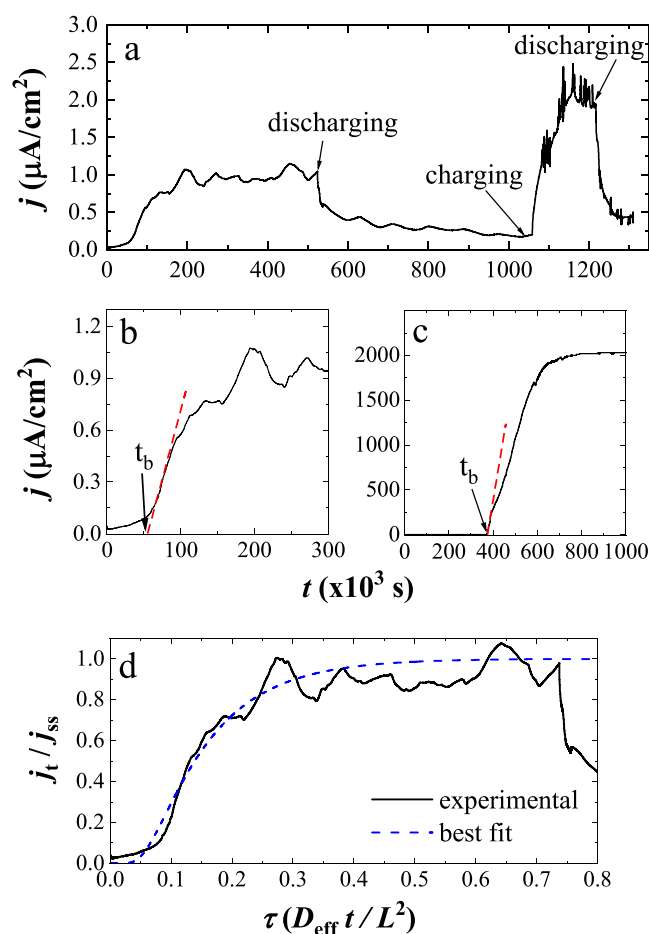
Fig. 2. EHP curves acquired at room temperature in a DS permeation cell filled with 0.1 M NaOH in both compartments. Hydrogen charging was carried out galvanostatically at -2 mA/cm^2. (a) Two charge/discharge cycles for wrought Ti-6Al-4V membrane. (b) First rise transient for wrought Ti-6Al-4V membrane. (c) First rise transient for EBM Ti-6Al-4V membrane. (d) Normalized current density vs. dimensionless time for wrought Ti-6Al-4V membrane. The dashed blue line is the best fit obtained from the theoretical Laplace series.

Table 1
D_{eff} derived from t_b (Eq. 6) and from the Laplace series fit (Eq. 4) of the experimental EHP transients obtained at room temperature, for wrought and EBM alloys, in comparison to D_{eff} values reported previously for wrought Ti-6Al-4V.

Alloy	t_b ($\times 10^3$ s)	D_{eff} ($\times 10^{-10}$ cm^2/s)	
		Experimentally, using t_b	Laplace fit
Wrought	38 ± 30[a]	3.10 ± 2.40[a]	1.70 ± 0.70[a]
EBM	320 ± 150[b]	0.35 ± 0.17[b]	
Ref.[44]	0.3	626	
Ref.[43]	0.046	3260	

[a] $n = 4$ samples.
[b] $n = 3$ samples.

significant effect on the hydrogen transport. For experimental transients that are steeper than that associated with Fick's second law, the effective diffusion coefficient can be calculated also based on the time lag, t_{lag} [33,40,49]. Since j_{ss} could not be determined for the EBM alloy, comparison between the diffusion coefficients based on t_b and t_{lag} is provided here only for the wrought alloy. The value of D_{eff} derived based on t_{lag} is $2.20 \pm 1.19 \times 10^{-10}$ cm^2/s, i.e. between the vales derived based on Laplace fitting and on t_b.

3.3. The role of the surface and microstructure

Fig. 3 shows SEM images of wrought and EBM Ti-6Al-4V alloys before the EHP test (i.e., before hydrogenation). The longitudinal cross-section of the wrought alloy is in the direction parallel to the extruded rod axis. The microstructure of the wrought alloy comprises of two phases – a primary α-phase (dark gray area in these SEM images), and a minor β-phase (light gray flakes). The microstructure looks different when comparing the longitudinal and transverse orientations. In the longitudinal orientation (Fig. 3a,b), the β-phase morphology is more aligned, which can be attributed to the direction of the extrusion process. On the other hand, in the transverse orientation the β-phase is discontinuous and unaligned. A similar microstructure was reported before [34]. In the case of the EBM alloy, the longitudinal cross-section is parallel to the build direction (and parallel to the hydrogen diffusion direction in EHP tests), while the transverse cross-section reveals the in-layer microstructure. The microstructure of the EBM alloy differs significantly from that of the wrought alloy; it exhibits a lamellar Widmanstätten microstructure, consisting of major α-phase separated by minor β-phase with fine needle-like morphology oriented in a crisscross pattern within the prior β columnar grains. The α-phase platelets look dark gray in the images, while the β-phase looks light gray (Fig. 3e–h). This morphology is typical of EBM Ti-6Al-4V [12–14,34,53]. Evidently, unlike in the wrought alloy, in the EBM alloy the β-phase forms a 3D continuous network and there are significantly more α/β interphase boundaries. In Fig. 3, both non-hydrogenated alloys are free of cracks and microvoids. Micro-computed tomography (μCT) imaging of the whole membranes did reveal in the EBM membrane a few micropores with diameters in the range of 10–25 μm; however, none of these penetrated the membrane.

The SEM images in Fig. 4 show longitudinal cross-sections of membranes made of wrought and EBM Ti-6Al-4V right <u>after</u> EHP experiments. The longitudinal cross-sections are in the hydrogen flux direction, which for the wrought alloy is parallel to the rod extrusion direction, while for the EBM alloy is in the build direction. Comparing the SEM images before and after hydrogenation, it is evident that the hydrogenated samples have undergone microstructural changes. In the case of the wrought alloy, during the hydrogen permeation test, the β-phase grains "aligned" themselves along the hydrogen diffusion direction. The β-grains have swollen and are rougher. Swollen and rougher grains are also observed in the EBM alloy, which also still retains the basket-weave microstructure. Similar morphologies in Ti-6Al-4V were related elsewhere to hydride phases [57,58]. In both alloys, these morphology transformations are not limited to the entry surface only, but are observed throughout the thickness of the membranes. Hydride formation seems to be accompanied by void formation (more so in the EBM alloy). Formation of microvoids around the α/β interphases in hydrogenated Ti-6Al-4V samples [19,28,29,34] was attributed to hydride precipitation from a hydrogen supersaturated phase [29]. It should be noted that macro-cracks were not detected in hydrogenated wrought alloy, not even after prolonged permeation experiments, but were observed in hydrogenated EBM alloy.

EDS analysis revealed the presence of Pd on the entry surface of all samples after EHP experiments. Following hydrogenation, the Ti concentration adjacent to the entry surface decreased, while the V concentration increased. This finding is consistent with prior reports [28,57,59], and can be related to α-to-β phase transformation. This transformation is controlled by the diffusion of vanadium, as the hydrogenation of the titanium alloy considerably enhances the self-diffusion of metal atoms and the diffusivity of dissolved atoms.

XRD was used to verify that hydride phases indeed were formed during EHP tests. Diffraction patterns were acquired both from the entry and from the exit surfaces after EHP experiments, and were compared to diffraction patterns from the surface of non-hydrogenated samples (Fig. 5). The non-hydrogenated samples exhibit the typical XRD pattern for Ti-6Al-4V, with two distinct phases – α-hcp (major) and β-bcc (minor). The reflections at 2θ = 35.5°, 38.6°, 40.6° correspond to the (100), (002), (101) reflections of the α-phase (ICDD PDF-04–002–8708), respectively. The peak at 39.9° corresponds to the (110) reflection of the β-phase (ICDD PDF-01–074–7075). Besides minor differences, which result from the different grain orientations, similar peaks appear in both alloys.

After EHP tests, the diffraction patterns vary mostly in the range of 34–43°. After EHP tests, the α-phase reflections (100), (002) and (101) are present with peak positions unchanged. This is expected given the
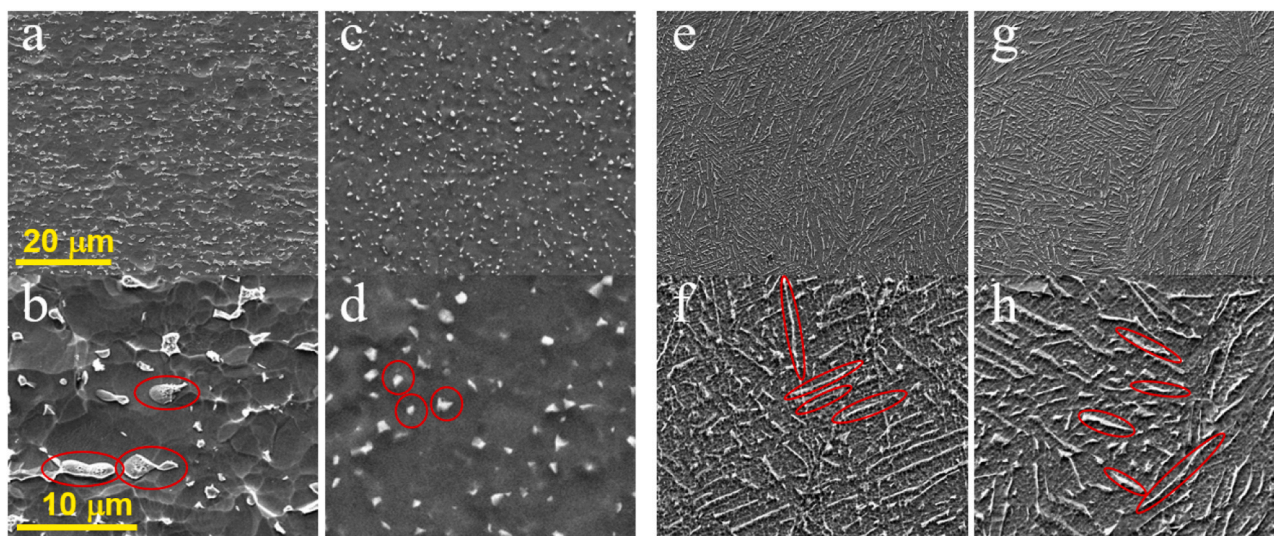

Fig. 3. SEM images of as-received wrought (a–d) and EBM (e–h) alloys cut in the longitudinal (a, b, e, f) and traverse (c, d, g, h) directions, at lower (top raw) and higher (bottom raw) magnifications. In (b–h) the β-phase grains (brighter area in the images) are encircled by red lines. Finer filamentous β-phase grains in (f, h) are more difficult to be distinguished and marked at this magnification. In all images, the darker gray area in between the brighter grains is of the main α-phase.
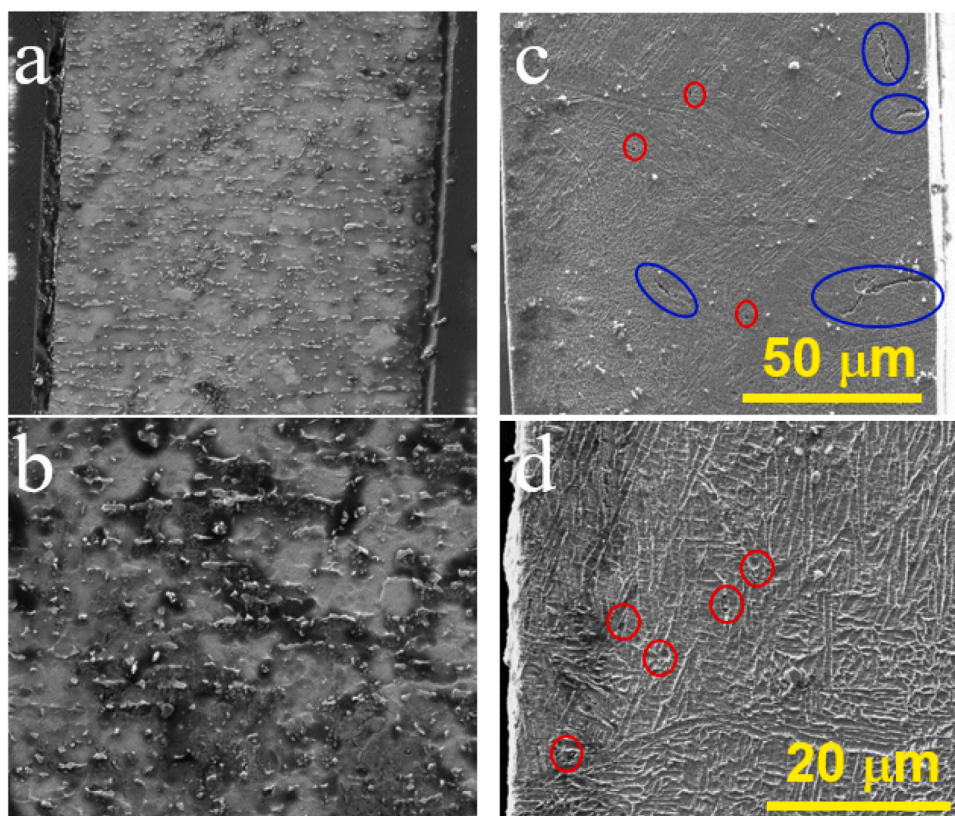
Fig. 4. SEM images of longitudinal cross-sections of wrought (a, b) and EBM (c, d) Ti-6Al-4V alloy membranes after the EHP experiments reported in Fig. 2. In all images, the entry side is on the left side. Top raw: lower magnification, bottom raw: higher magnification. Microvoids are encircled in red, microcracks are encircled in blue (c, d).

low solubility of hydrogen in the α-phase [20,21,59]. In contrast, the β(110) peak shifts to lower angle (39.5° and 38.8° for the wrought and EBM alloys, respectively) compared to the non-hydrogenated samples (39.9°). This shift reflects lattice expansion of the β-phase as the β$_H$ solid solution is formed [60]. The more significant shift of the β(110) peak in the case of the EBM alloy reflects higher content of dissolved hydrogen, in agreement with previous reports [21,26,28,34,57]. The lattice expansion due to hydrogenation is expected to increase internal microstrains [29].

In addition to the β-phase lattice expansion, new peaks were detected at 36.5°, 37.7° and 42.1° on either the entrance side or both sides of the hydrogenated samples. These peaks could not be matched with reported phases in the International Center for Diffraction Data (ICDD). Navi et al. [26,28] were the first to relate these peaks to hydride phases and marked them δ$_a$ and δ$_b$. These hydrides are variants of the δ (TiHx) phase and are characterized by fcc unit cell and $Fm\bar{3}m$(225) space group. It was suggested that δ$_a$ and δ$_b$ phases are formed during hydrogenation by the transformation of the α-phase into hydrides. The diffraction peaks corresponding to δ$_a$ and δ$_b$ in both alloys can be detected on both sides of the membranes, although both phases and β$_H$ were more pronounced at the entry side. The presence of these phases at the exit side confirms that hydrogen has indeed penetrated the membrane entirely. Comparison was made between different wrought alloys after EHP tests. It was found that samples with higher hydrogen permeation currents contained more hydride phases at the entrance surface, and more pronounced β$_H$ phase at the exit surface. The appearance of large hydride peaks at the entry side matched significant morphological changes at the entry side in the cross-section SEM images.

In the EBM alloy, the δ$_a$ and δ$_b$ peak intensities are higher than in the wrought alloy, implying that the amount of hydrides in the EBM alloy is greater than in the wrought alloy. The δ$_a$ and δ$_b$ peaks are also much broader in the EBM alloy, suggesting that the hydride grains are smaller or are stressed. Another important difference in the XRD patterns of hydrogenated EBM and wrought alloys is the broadening of the peaks corresponding to the α-phase. This broadening can be ascribed to one or more of the following reasons: (1) α-grain refinement [60] and/or due to residual internal stress [57,59]. (2) α-to-α$_2$ (TiAl$_3$) phase transformation [14,58,61]. (3) δ-TiH$_{1.5}$ hydride phase formation. (4) α-to-α$_H$ transformation [59]. (5) Domain size refinement [26]. The fact that peak broadening is common to all α(101), α(002) and α(101) diffraction peaks suggests that grain (or domain size) refinement and/or internal stress in the α-phase are at least partially responsible. However, since the broadening is significantly more pronounced for the α(101) peak at ca. 41°, where the δ-TiH$_{1.5}$(200) peak is expected [14,57,61–63], it is reasonable to assume that hydride formation is also responsible to the peak broadening at ca. 41° in the EBM alloy during EHP.

Table 2 summarizes the phase content and lattice parameters obtained using TOPAS Rietveld refinement software (all R_{wp} values were below 13.198). The values in Table 2 for the EHP-tested samples are presented as a range of values for three membranes of each alloy. For the non-hydrogenated samples, the β-phase content is approximately 4 wt% in the wrought alloy and 5 wt% in the EBM alloy. While in the wrought alloy the β-phase relative content increased due to hydrogenation, in the EBM alloy it decreased. The increase in the β-phase content has been attributed to an α$_H$-to-β$_H$ phase transformation due to the β-stabilizing nature of hydrogen [14]. From Table 2 one learns also that hydrogenation leads to an expansion of the lattice parameter of the β-phase due to the formation of the β$_H$ solid solution. The expansion of the β-phase is significantly greater in the EBM alloy than in the wrought alloy. Consequently, the β-phase peak overlaps with the α(200) peak. Hence, there is some uncertainty in the calculated weight percentage of the β-phase in the EBM alloy. One could compare, however, the change in the α-phase content in the two alloys due to hydrogenation. At the entry
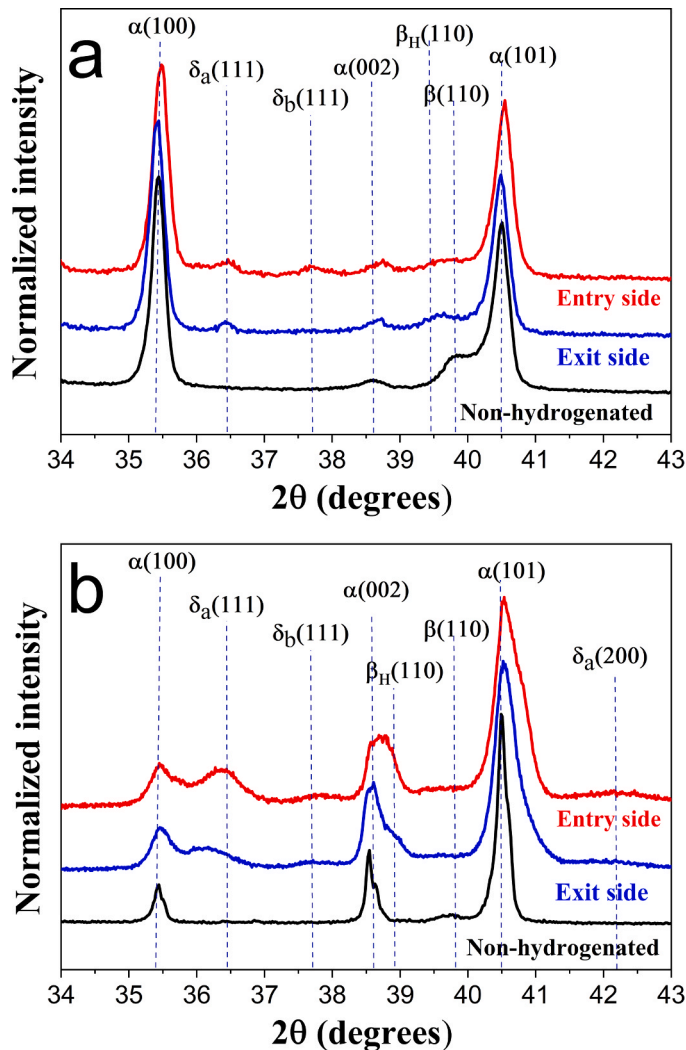
Fig. 5. XRD patterns obtained from the surface of wrought (a) and EBM (b) Ti-6Al-4V membranes before (black lines) and after (blue and red lines) EHP experiments.

side, the α-phase content is more affected in both alloys than at the exit side, and it changes from 96% to 72% on average and from 95% to 82% on average in the wrought and EBM alloys, respectively.

At the exit side, the α-phase content changes to 92% and to 88% on average in the wrought and EBM alloys, respectively. Clearly, the difference in the α-phase content at the entry and exit sides after EHP experiments is much more pronounced in the wrought alloy than in the EBM alloy. In fact, considering the scatter of results, one can claim that in the EBM the α-phase content is nearly the same at both sides of the membrane. One should, however, be cautious interpreting the α-phase content values for the EBM alloy since, as mentioned above, significant broadening of the α-phase peaks is observed exclusively in the hydrogenated EBM alloy (Fig. 5b). This broadening suggests that a significant portion of the original α-phase has been transformed into α_H, α_2 (TiAl$_3$), or δ-TiH$_{1.5}$ phase. All three phases have overlapping peaks, thus it is impossible to precisely quantify the content of residual α-phase.

Another notable difference between the two alloys is the additive content of the two hydride phases δ_a and δ_b. While at the entry sides, the content of the hydrides is on average similar (20.5% and 14.5% for the wrought and EBM alloys, respectively), at the exit side the average hydrides contents are significantly different (0.9% and 8.8% for the wrought and EBM alloys, respectively). The EBM alloy exhibits a more uniform distribution of hydrogen in the form of hydrides across the membrane. It was previously reported [28] that hydrides are products of α-phase transformation, and indeed, one can see that there is a good correlation between the reduced α-phase content and the increased $\delta_a + \delta_b$ phases content, and this correlation holds throughout the membrane thickness in both alloys.

The distribution of hydrogen in the longitudinal cross-sections of the membrane samples after EHP experiments was studied using ToF-SIMS and AES. Fig. 6a,b and Fig. 6c,d show the ToF-SIMS results for wrought and for EBM alloys, respectively. The images show the distribution maps of total hydrogen (Fig. 6a,c) and of titanium hydrides (Fig. 6b,d). For the total hydrogen distribution maps, the signals of the masses corresponding to the negative ions H$^-$ and TiH$_x^-$ ($x = 1$–5) are combined. For the distribution maps of titanium hydride, the signals of the negative TiH$_x^-$ ions only are combined. Brighter regions in the images correspond to stronger hydrogen or titanium hydride signals, as indicated by the scale bar. The total hydrogen intensity detected by ToF-SIMS analysis includes contributions from several hydrogen sources, such as solid-solution hydrogen, hydrides, surface-adsorbed hydrogen, and contaminations. When all other contributions are filtered out, the intensity corresponding solely to hydrides is obtained.

Qualitatively, in both alloys the corresponding total hydrogen and

Table 2

Phase contents and lattice parameters in wrought and EBM Ti-6Al-4V alloys before and after EHP experiments, calculated using TOPAS Rietveld refinement software. The nominal error in the estimated wt% is < 1.5%. The reported range of results with samples after EHP are for 3 samples of each alloy type.

| Alloy	Condition	Sample side	α/α$_H$	β/β$_H$	δ$_a$	δ$_b$
Wrought	Before EHP		96.03 wt% $a = 2.924$ Å $c = 4.672$ Å	3.97 wt% $a = 3.191$ Å		
	After EHP	Entry	57.47–86.96 wt% $a = 2.925$–2.928 Å $c = 4.672$–4.683 Å	5.87–11.58 wt% a = 3.179–3.212 Å	3.77–16.82 wt% $a = 4.279$–4.297 Å	1.29–15.04 wt% $a = 4.134$–4.140 Å
		Exit	89.53–95.05 wt% $a = 2.925$–2.928 Å $c = 4.668$–4.671 Å	4.70–8.78 wt% $a = 3.200$–3.210 Å	0–0.90 wt% $a = 4.270$–4.317 Å	0–0.79 wt% $a = 4.136$ Å
EBM	Before EHP		94.92 wt% $a = 2.924$ Å $c = 4.668$ Å	5.08 wt% $a = 3.206$ Å	-	-
	After EHP	Entry	78.17–86.87 wt% $a = 2.924$–2.928 Å $c = 4.664$–4.669 Å	2.26–4.82 wt% $a = 3.208$–3.231 Å	10.14–5.04 wt% $a = 4.296$–4.300 Å	4.55–9.43 wt% $a = 4.156$–4.203 Å
		Exit	85.46–90.03 wt% $a = 2.922$–2.928 Å $c = 4.662$–4.672 Å	3.14–4.40 wt% $a = 3.196$–3.244 Å	3.22–5.82 wt% $a = 4.303$–4.323 Å	3.10–5.53 wt% $a = 4.211$–4.265 Å
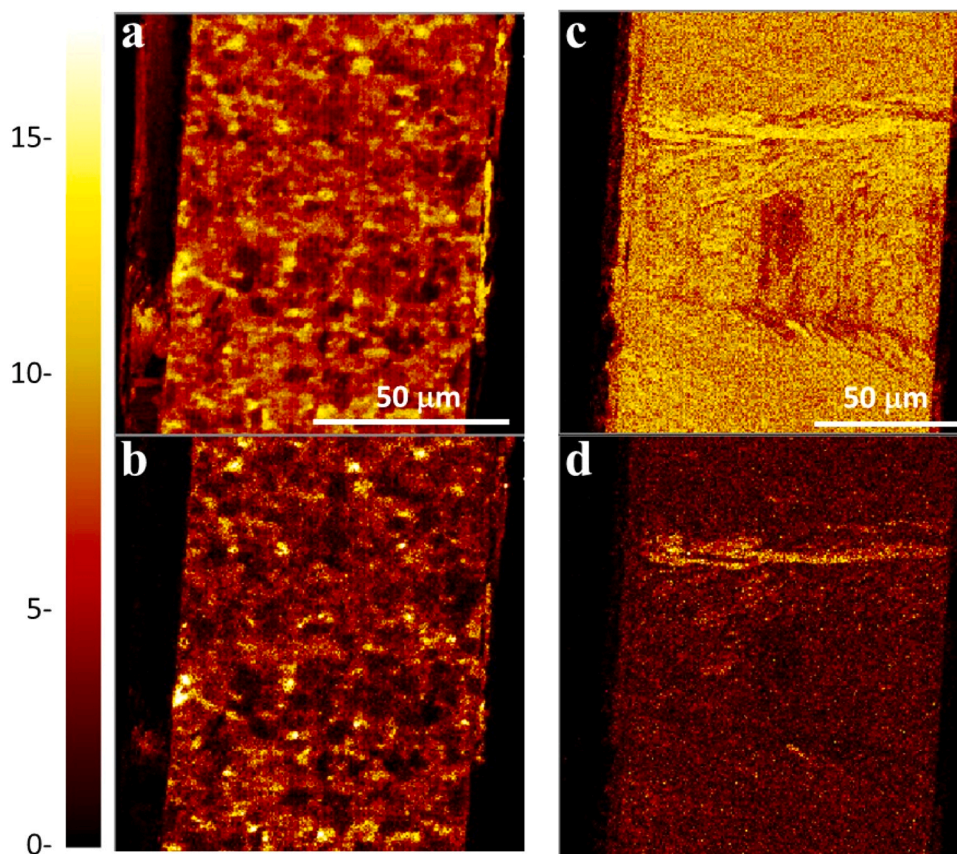
Fig. 6. ToF-SIMS mapping images in longitudinal cross-sections of (a, b) wrought, and (c, d) EBM alloy membranes after EHP experiments. (a, c) are total hydrogen maps, (b, d) are hydrides only maps.

hydride distribution maps are quite similar (with different overall intensity), which means that there is a clear correlation between the distribution of total hydrogen and that of hydrides. This correlation has two implications: (1) the contribution of contaminations is negligible; (2) solid-solution and hydrides feed each other and their hydrogen concentrations are probably in equilibrium with each other. Since the hydrides' signal is much weaker than the total hydrogen signal, we exclude the possibility that it is the dominant component and that it overshadows the total hydrogen signal. It should be emphasized that no calibration was attempted in the ToF-SIMS analysis and therefore, the color scale represents relative intensities only. As a result, comparisons of hydrogen or hydride intensities in two different samples should be avoided.

Hydride layers were detected on the entry side of all wrought membranes, although on some membranes they were continuous, thick (ca. 10 μm), and covered laterally the whole surface, whereas on other membranes they were discontinuous and much thinner. Apparently, in extreme cases when the hydride layer was thick enough (>10 nm) and continuous, it served as an efficient surface barrier, impeding hydrogen permeation through the membrane. In those cases, no permeation current was detected. Another correlation between the EHP and the ToF-SIMS data was that higher permeation currents were associated with higher ToF-SIMS total hydrogen and titanium hydrides intensities in the bulk of the membrane.

Fig. 6a,b shows hydrogen distribution in the wrought alloy. Apparently, hydrogen is concentrated in isolated clusters across the whole membrane, suggesting that hydrogen tends to accumulate in preferred sites. Since the variations in local hydrogen concentrations throughout the sample correlates to the spatial distribution of β-phase grains (as depicted in the SEM cross-section images in Fig. 3), it may be concluded that the hydrogen-rich regions in the ToF-SIMS maps of the wrought

alloy membrane are α/β interphase boundaries [18,27]. Clustering of hydrogen and hydrides at interfaces other than α/β interphase boundaries have been reported for hydrogenated titanium [22].

Fig. 6d,e shows the ToF-SIMS maps of total hydrogen and titanium hydride across an EBM alloy membrane. The lamellar microstructure of the EBM alloy can be partially resolved in the image. Unlike hydrogen clustering in the wrought alloy, the distributions of total hydrogen and of hydrides in the EBM alloy are much more uniform across the membrane. Apparently, hydrogen permeates and is distributed more efficiently in the EBM alloy than in the wrought alloy. This is most likely due to the fine lamellar microstructure in the EBM alloy, with its continuous β-phase network, which provides a more rapid pathway for hydrogen diffusion [14,28,64]. The finer microstructure of the EBM alloy also implies ample of grain boundaries, which act as hydrogen traps.

As mentioned above, the EBM membranes were cracked during EHP experiments. These cracks were clearly noticed in micro-CT movies made of scans through the membrane thickness. Fig. 7 shows ToF-SIMS hydrogen distribution maps acquired near a crack in an EBM alloy membrane after EHP experiment. Clearly, a high concentration of total hydrogen and of hydrides is observed adjacent to the crack and could explain its initiation and propagation. Interestingly, oxygen is also detected along the primary crack as well as along secondary cracks (Fig. 7c). Although the contribution of Ti-oxide to the total oxygen signal is limited (Fig. 7d), one cannot exclude the possibility that oxygen was involved in crack initiation and propagation.

To complement the chemical composition analysis, AES analysis of membranes before and after EHP tests was carried out too. The titanium LMM transition lines at around 380 and 420 eV were obtained and compared also with those of TiH_2 powder (a calibration sample). Fig. 8 presents the differential AES spectra obtained for wrought and EBM
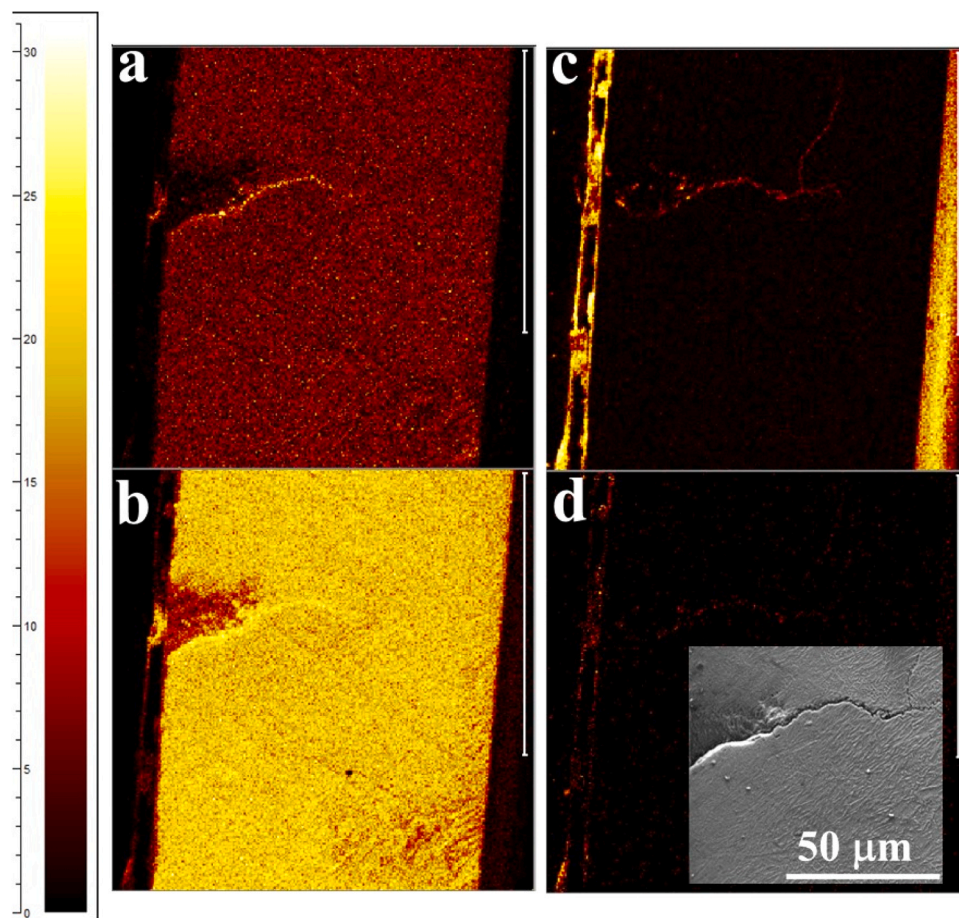
Fig. 7. ToF-SIMS cross-section mapping of total hydrogen (a), hydride (b), oxygen (c), and TiO (d) contents around a crack that formed in EBM Ti-6Al-4V membrane during EHP experiment. In all images, the entry surface is on the left side and each scale bar equals 100 μm. The intensity bar on the left is in arbitrary units. The inset in (d) is a SEM image of the same membrane sample at the same region.

alloys before and after EHP experiments. The differential AES spectrum of TiH$_2$ powder is presented in Fig. 8c. The AES measurements were taken in few discreet steps across the membrane thickness in the longitudinal cross-section of the membranes.

It has been previously shown that AES can differentiate between various Ti-based compounds, including TiH$_2$ [65], by analyzing the titanium peaks. Apparently, in the differential AES spectrum for TiH$_2$, the titanium positive peak at 374.8 eV is suppressed while the positive peak at 411.1 eV is enhanced relative to the intensities for pure titanium. Accordingly, the ratio between the intensities of the suppressed peak and the enhanced one is expected to be a good measure of the degree of hydride transformation. To avoid errors due to noise and unstable baselines, each peak intensity was measured vs. the corresponding negative peak intensity. In Fig. 8b, the relevant peaks are indicated with blue and red triangles. The peaks ratio is the ratio between the intensity difference between the two blue peaks and the difference between the two red peaks. To determine the concentration of TiH$_2$, the normalized peaks ratio was calculated using the lever rule:

The above calculation procedure to determine the degree of hydride conversion, i.e. the value of x in TiH$_x$, was developed in this study. The normalized ratio is used to overcome the fact that alloys, and not pure titanium, are used, and non-hydrogenated alloy samples should be taken as reference. The outcome of the analysis is illustrated in Fig. 8f, which displays the normalized peak ratios at each step along the sample thickness, from the entry surface to the exit surface, for two wrought and two EBM membrane samples. The y-axis in Fig. 8f indicates the amount of titanium transformed into TiH$_2$, or how close the stoichiometry at each step to TiH$_2$ is. The value of 1 corresponds to complete transformation of Ti to TiH$_2$.

In general, EBM alloy samples exhibit after EHP experiments a higher degree of hydride bonds formation compared with wrought alloy samples, in agreement with the ToF-SIMS results. Since the primary electron beam spot diameter (50 nm) is small compared to the Ti-6Al-4V grains, the value at an individual measurement point is highly dependent upon the specific grain. The fluctuations seen with wrought samples are
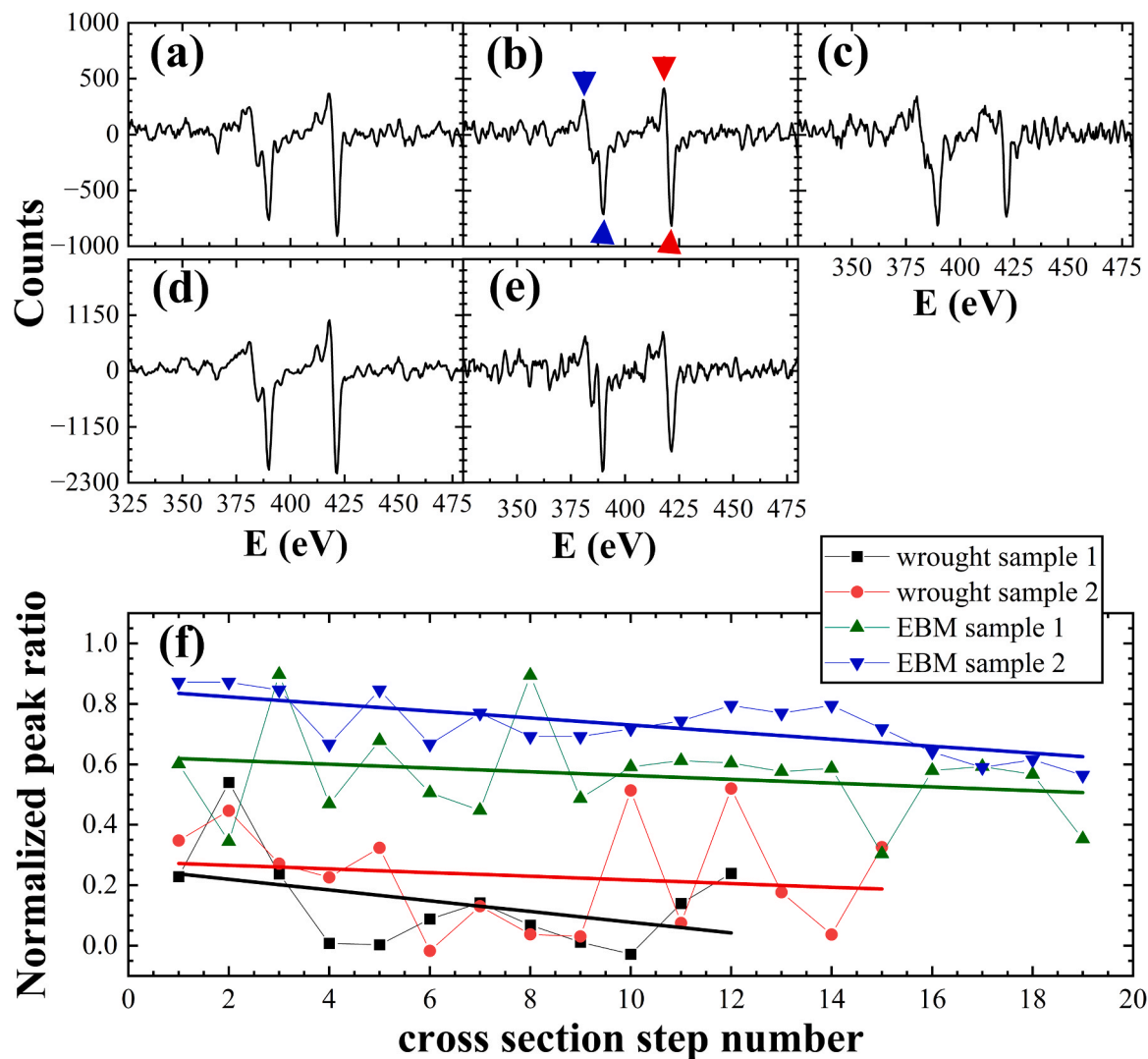
$$NR = \frac{(\text{peaks ratio in hydrogenated sample}) - (\text{peaks ratio in non} - \text{hydrogenated sample})}{(\text{peaks ratio in TiH}_2 \text{ sample}) - (\text{peaks ratio in non} - \text{hydrogenated sample})} \tag{11}$$

Fig. 8. AES differential spectra (a–e) obtained before (a, b) and after (d, e) EHP experiments. (a, d) wrought alloy, (b, e) EBM alloy. (c) AES differential spectrum obtained using TiH$_2$ standard calibration powder. (f) Summary of the normalized peak ratios obtained from multi-step measurements across the thickness of two wrought (blue and green lines and symbols) and two EBM (red and black lines and symbols) membranes. The symbols and jugged lines are the measured values, while the thick lines are linear fit of the experimental results. The difference in the number of steps in the different samples is related to different sample thicknesses. The blue and red triangle arrows in (b) mark the differential peaks used to derive the peaks ratios (see text).

greatly reduced with EBM alloy samples thanks to the finer microstructure and smaller grain size in the EBM alloy, and most probably due to the more homogeneous distribution of hydrogen in the EBM alloy. To gain a better visualization of the results, trend-lines (of the same respective colors) are also shown in Fig. 8f. For both types of samples, the entry surface exhibited higher content of TiH$_2$ compared to the exit side. Moreover, the EBM samples displayed a less steep trend, indicating a more homogeneous content of TiH$_2$ across the membrane thickness.

It is interesting to compare the degree of TiH$_2$ hydride bond formation found by AES analysis to the phase content found by XRD Rietveld refinement. For the wrought alloy at the entry side, the degree of hydride bond formation is 20–25%, in close agreement with the sum of δ_a and δ_b hydride phase contents found by Rietveld analysis (see Table 2). For the EBM alloy at the entry side, the degree of hydride bond formation is > 60%, while the sum of δ_a and δ_b hydride phase contents found by Rietveld analysis is only < 10%. This discrepancy may be attributed to the fact that hydride content by XRD depends on the crystallinity of the hydride phase. Amorphous, not fully structured hydrides would not be manifested in the XRD. In contrast, in AES the signal intensity represents the amount Ti-H$_2$ bonds, and is not sensitive to the crystallinity, and therefore – detection of not fully ordered hydrides is plausible.

Another possible reason for the discrepancy is that some of the crystalline hydride is not accounted for in XRD analysis due to overlapping diffraction peaks. For example, the profound $\alpha(101)$ diffraction peak broadening at around $2\theta = 41°$ in the diffraction pattern of the EBM alloy may be attributed to a δ-TiH$_{1.5}$ phase, which was not accounted for in the total hydride content calculated by Rietveld refinement in Table 2. The fact that the discrepancy between the XRD and the AES analysis arises only in the case of the EBM alloy is an indication that EBM Ti-6Al-4V is subjected to more extensive phase transformations, which are driven by a more uniform hydrogen distribution and a faster local hydrogen accumulation up to a critical concentration, unlike the wrought alloy.

4. Discussion

Despite the widespread use of titanium and its alloys, including in hydrogen-containing atmospheres, very little has been published on electrochemical hydrogen permeation in these structural materials. We believe that the main reason for this is the necessity for exceptionally careful experimental procedure. First, the native oxide layer on the titanium membranes, which acts as a strong diffusion barrier both to

hydrogen entry and to hydrogen exit, must be avoided on both sides of the membrane. If a titanium oxide layer is covered with Pd on the entry side, this oxide might not be reduced as needed to circumvent its barrier properties, and consequently hydrogen entering Pd may not be transmitted through the oxide into the alloy. Second, the rapid formation of a titanium hydride layer on the entry side establishes a new surface barrier to hydrogen entry, which is also brittle and serves as a preferred site for initiation of microcracks that affect the permeation current transients and lead to sample disintegration. Third, hydrogen traps exist in the microstructure of the dual-phase Ti-6Al-4V alloy. All of these result in a non-classical (sigmoidal) permeation curve and in inability to run several cycles with repeatable results.

Given the above, the first stage in this work was to establish a good procedure for sample preparation and to identify proper conditions for EHP tests of Ti-6Al-4V alloy. The native titanium oxide layer on the surface of the membranes was first removed, and immediately afterwards the samples were stored, transferred and handled under vacuum atmosphere to prevent reoxidation, until a protective Pd coating was applied. Once a significant effect of the membrane thickness was verified experimentally (thick membranes making the experiments impractically long), all membranes were thinned down to 90–100 μm, making the final radius-to-thickness ratio ca. 40. The need for Pd coating on both sides of the membrane was verified experimentally; 20 ± 1 nm Pd film was applied on each side of the membrane. Evaluation of several electrolytes led to the conclusion that the use of argon-purged 0.1 M NaOH without surface poisoner as both catholyte and anolyte results in reliable permeation curves. Based on cyclic voltammetry tests, a constant reduction current density of -2 mA/cm^2 at the entry side and a constant potential of $+ 0.15$ V vs. Hg/HgO/0.1 M NaOH reference electrode at the exit side were selected.

Working with Pd-coated membranes, one could argue that hydrogen might be trapped at the interface between the substrate and the coating [66] and recombine into H$_2$ molecules, leading to volume expansion, bubble/blister formation, and delamination of Pd. However, this was not the case in this study, since EDS identified the presence of the Pd coating at the entry side of all samples after EHP tests. On the other hand, the color of the membrane changed during EHP tests, to yellow-blueish on the entry side and matte gray on the exit side. If 20 nm thick Pd film is transparent in visible light, this color change could be indicative of the formation of either titanium hydride (on the entry side) or titanium oxide (on the exit side). The thickness of the newly formed surface layer and the oxidation state of titanium in it would dictate different colors [67,68]. It has been reported [69] that Pd is transparent to light at wavelengths of 500–1100 nm (that overlap with the wavelength of visible light, 380–700 nm) up to a thickness of 45 nm. If the 20 nm thick Pd film is not transparent to visible light, however, the color change should be associated with interactions between Pd itself and hydrogen. Hydrogen was found to change the optical transparency of the Pd film, reflecting first-order phase transitions [69]. The rate of the hydrogen-induced change in the transparency of layers linearly increased with increasing hydrogen concentration in the environment [69]. Both Ti and Pd have been shown to have dynamically tunable optical properties when exposed to hydrogen [70]. One way or another, it is beyond the scope of this work to study the origin of color change.

The effective diffusion coefficients of hydrogen in wrought and EBM Ti-6Al-4V were successfully and reliably determined by EHP experiments. In both cases, the breakthrough time (t_b) method was employed to the first rise current transient. In the case of the wrought alloy only, the more classical shape of the permeation curve allowed to also deduce the diffusion coefficient from Laplace series sigmoidal function fitting. Thus, the average effective diffusion coefficient at room temperature was found to be 3.1×10^{-10} cm^2/s for the wrought alloy, an order of magnitude faster than 3.5×10^{-11} cm^2/s for the EBM alloy. These values are much lower than the values of 3.26×10^{-7} cm^2/s and 6.26×10^{-8} cm^2/s reported before in Refs. [43,44], respectively. It should also be noted that hydrogen diffusion coefficients of 1×10^{-7} and 1×10^{-10}

cm^2/s have been reported for β-titanium and α-titanium, respectively [21,24,71]. Since the wrought and EBM Ti-6Al-4V alloys in this study contained 96 and 95 wt% α-phase, respectively, one should expect D_{eff} of the order of 1×10^{-10} cm^2/s, as measured in this study.

The higher diffusivity in the wrought alloy compared to the EBM alloy might look surprising if taking into account only the higher density of α/β interphase boundaries in the Widmanstätten microstructure of the EBM alloy and referring to them as short circuits for hydrogen diffusion. However, if considering also hydride formation at the entry surface and in the bulk of the alloy membranes and hydrogen traps in both alloys, the lower hydrogen diffusivity in the EBM alloy can be explained based on SEM, XRD, ToF-SIMS and AES data. A correlation was found between the permeation current transient and the microstructure. The lamellar microstructure of the EBM alloy provides abundance of both reversible and irreversible trapping sites, mainly at α/β interphase boundaries [27]. The outcome of the abundance of traps is threefold: (1) acting as sinks, the traps inhibit hydrogen diffusivity; (2) traps provide ample supply of hydrogen atoms to form hydrides; (3) traps provide ample supply of hydrogen to exceed the critical concentration for brittle crack initiation. The first two effects are probably the reason why D_{eff} is much smaller in EBM and why permeation currents were virtually undetected in EBM alloy membranes, once they were sufficiently hydrogenated. The third effect explains the fast cracking and failure of EBM alloy membranes during EHP experiments. One can anticipate that under similar electrochemical hydrogenation conditions, an EBM Ti-6Al-4V alloy will be more susceptible to hydrogen embrittlement than a wrought alloy.

XRD revealed a significantly higher δ$_a$ and δ$_b$ hydrides content on the entry surface of the EBM alloy compared to the wrought alloy. AES revealed a significantly higher degree of hydride bond formation at the surface of the EBM alloy compared to the wrought alloy, and also significantly higher than in XRD analysis. We believe that the higher degree of hydride bond formation is due to TiH$_{1.5}$ formation, which is supported by significant peak broadening around $2\theta = 41°$, detected only in the EBM alloy. As a result of the significantly higher hydrides content at the surface of the EBM alloy, its membranes exhibited considerable brittleness, and microcracks formed in them during EHP tests. Thicker and more continuous hydride layers at the entry side serve as a more efficient barrier to hydrogen transport through the membrane. The microstructure of the EBM membranes changed significantly due to hydrogenation. First, the dual-phase microstructure was almost wiped away in the hydrogenated EBM samples not only near the entry surface, but also in the bulk membrane and near its exit surface. Such microstructural change can take place via two mechanisms: (1) Fragmentation of laths and microstructure refinement, where the grain boundaries of plates and the lamellar structure disappear. This kind of behavior upon hydrogenation was attributed by Pushilina et al. [57] to the migration of primary α-plate grain boundaries due to β-grain boundaries growth. This transformation occurs at the early stages of hydrogenation. (2) Hydride formation, where hydride phases nucleate at the α/β interphase boundaries, resulting in smoothing out of the β-phase network [28,35, 57]. In addition, microvoids and microcracks are noticed in the bulk of the EBM samples. These pronounced microstructural changes in EBM samples imply that the EBM alloy is more susceptible to hydrogen embrittlement than the wrought alloy. While hydrides act as irreversible hydrogen traps, grain boundaries are known to act as reversible traps [35,59,64,72]. The abundance of grain/interphase boundaries thus has inhibitive effect on hydrogen diffusion in the EBM alloy, and consequently could promote hydrogen embrittlement.

5. Conclusions

The electrochemical hydrogen permeation (EHP) through wrought and electron beam melted (EBM) Ti-6Al-4V alloys was analyzed and compared. A thorough chemical and microstructural characterization was carried out to explain the EHP characteristics and the difference in the behavior of the two alloys. A careful procedure for sample

(membrane) preparation and proper EHP conditions were established in order to minimize the effect of titanium oxide surface layer as hydrogen diffusion barrier and obtain permeation curves that would enable reliable determination of the diffusion coefficient. The following conclusions were drawn:

1. The effective diffusion coefficients were successfully and reliably determined, employing the breakthrough time method. The average effective diffusion coefficient at room temperature is 3.1×10^{-10} cm^2/s for the wrought alloy and 3.5×10^{-11} cm^2/s for the EBM alloy. These values make sense as the wrought and EBM Ti-6Al-4V alloys in this study contained 96 and 95 wt% α-phase, respectively.
2. The higher hydrogen diffusivity in the wrought alloy compared to the EBM alloy results from different characteristics of the hydride layer that forms on the entry side of the membrane during EHP (namely, stronger surface barrier on the EBM alloy) and more irreversible traps in the microstructure of the EBM alloy.
3. The EBM alloy was found to be more susceptible to hydrogen embrittlement and cracking than the wrought alloy. Crack initiation and propagation was related to local high concentration of total hydrogen and of hydrides.

CRediT authorship contribution statement

Eliaz Noam: Conceptualization, Funding acquisition, Methodology, Project administration, Resources, Supervision, Visualization, Writing – review & editing. **Hayoun May:** Data curation, Formal analysis, Investigation, Writing – original draft. **Sabatani Eyal:** Conceptualization, Data curation, Formal analysis, Investigation, Methodology, Supervision, Visualization, Writing – original draft. **Shekhter Pini:** Data curation, Formal analysis, Investigation, Methodology, Resources, Visualization, Writing – review & editing. **Lulu-Bitton Noa:** Formal analysis, Writing – review & editing. **Navi Nissim U.:** Funding acquisition, Project administration, Writing – review & editing.

Data availability

Data will be made available on request.

Acknowledgements

Declaration of competing interest

The authors declare that they have no known competing financial interests or personal relationships that could have appeared to influence the work reported in this paper.

References

[1] J.C. Williams, R.R. Boyer, Opportunities and issues in the application of titanium alloys for aerospace components, Metals 10 (6) (2020) 705.
[2] C. Veiga, J.P. Devim, A.J.R. Loureiro, Properties and applications of titanium alloys: a brief review, Rev. Adv. Mater. Sci. 32 (2012) 133–148.
[3] N. Eliaz, Corrosion of metallic biomaterials: a review, Materials 12 (2019), 407 (article).
[4] V.A. Kumar, R.K. Gupta, M.J.N.V. Prasad, S.V.S. Narayana Murty, Recent advances in processing of titanium alloys and titanium aluminides for space applications: a review, J. Mater. Res 36 (2021) 689–716.
[5] G. Welsch, R. Boyer, E. Collings, Materials properties handbook: titanium alloys, ASM International, Mater. Park, OH (1994).
[6] R. Ding, Z. Guo, A. Wilson, Microstructural evolution of a Ti-6Al-4V alloy during thermomechanical processing, Mater. Sci. Eng. A 327 (2) (2002) 233–245.
[7] G. Lutjering, J.C. Williams, A. Glyser, Microstructure and mechanical properties of titanium alloys, in: J.C.M. Li (Ed.), Microstructure and Properties of Materials, World Scientific, Singapore, 2000, pp. 1–77.
[8] T.S. Tshephe, S.O. Akinwamide, E. Olevsky, P.A. Olubambi, Additive manufacturing of titanium-based alloys- a review of methods, properties, challenges, and prospects, Heliyon 8 (3) (2022), e09041.
[9] S.Y. Liu, Y.C. Shin, Additive manufacturing of Ti6Al4V alloy: a review, Mater. Des. 164 (2019), 107552.
[10] S.S. Al-Bermani, M.L. Blackmore, W. Zhang, I. Todd, The origin of microstructural diversity, texture, and mechanical properties in electron beam melted Ti-6Al-4V, Met. Mater. Trans. A 41 (13) (2010) 3422–3434.
[11] S.P. Narra, R. Cunningham, J. Beuth, A.D. Rollett, Location specific solidification microstructure control in electron beam melting of Ti-6Al-4V, Addit. Manuf. 19 (2018) 160–166.
[12] A. Safdar, L.Y. Wei, A. Snis, Z. Lai, Evaluation of microstructural development in electron beam melted Ti-6Al-4V, Mater. Charact. 65 (2012) 8–15.
[13] H.K. Rafi, N.V. Karthik, H.J. Gong, T.L. Starr, B.E. Stucker, Microstructures and mechanical properties of Ti6Al4V parts fabricated by selective laser melting and electron beam melting, J. Mater. Eng. Perf. 22 (12) (2013) 3872–3883.
[14] N. Pushilina, M. Syrtanov, E. Kashkarov, T. Murashkina, V. Kudiiarov, R. Laptev, A. Lider, A. Koptyug, Influence of manufacturing parameters on microstructure and hydrogen sorption behavior of electron beam melted titanium Ti-6Al-4V alloy, Materials 11 (5) (2018) 763.
[15] Y. Zhu, et al., Hydriding of titanium: Recent trends and perspectives in advanced characterization and multiscale modeling, Curr. Opin. Solid State Mater. Sci. 26 (6) (2022), 101020.
[16] P. Cotterill, The hydrogen embrittlement of metals, Prog. Mater. Sci. 9 (4) (1961) 205–250.
[17] W.M. Gao, W.Q. Li, J. Zhou, P.D. Hodgson, Thermodynamics approach to the hydrogen diffusion and phase transformation in titanium particles, J. Alloy. Compd. 509 (5) (2011) 2523–2529.
[18] H.J. Liu, L. Zhou, P. Liu, Q.W. Liu, Microstructural evolution and hydride precipitation mechanism in hydrogenated Ti-6Al-4V alloy, Int J. Hydrog. Energy 34 (23) (2009) 9596–9602.
[19] N. Lulu-Bitton, N.U. Navi, B.A. Rosen, S. Haroush, E. Sabatani, Y. Eretz-Kdosha, G. Agronov, N. Eliaz, The influence of gaseous hydrogen charging on the microstructural and mechanical behavior of electron beam melted and wrought Ti–6Al–4V alloys using the small punch test, Int J. Hydrog. Energy 48 (87) (2023) 34077–34093.
[20] F. Hua, K. Mon, P. Pasupathi, G. Gordon, D. Shoesmith, A review of corrosion of titanium grade 7 and other titanium alloys in nuclear waste repository environments, Corrosion 61 (10) (2005) 987–1003.
[21] J. Gu, D. Hardie, Effect of hydrogen on structure and slow strain rate embrittlement of mill annealed Ti6Al4V. Mater. Sci. Technol. 12 (10) (1996) 802–807.
[22] L. Yan, S. Ramamurthy, J.J. Noel, D.W. Shoesmith, Hydrogen absorption into alpha titanium in acidic solutions, Electro Acta 52 (3) (2006) 1169–1181.
[23] J.M. Howe, M.M. Tsai, Discussion of "on the mechanism of hydride formation in α-Ti alloys" by H.Z. Xiao, Scr. Met. Mater. 28 (4) (1993) 533–535.
[24] H.J. Christ, M. Decker, S. Zeitler, Hydrogen diffusion coefficients in the titanium alloys IMI 834, Ti 10-2-3, Ti21S, and alloy C, Met. Mater. Trans. A 31 (6) (2000) 1507–1517.
[25] I.I. Phillips, P. Poole, L.L. Shreir, Hydride formation during cathodic polarization of Ti.2. Effect of temperature and pH of solution on hydride growth, Corros. Sci. 14 (9) (1974) 533–542.
[26] N.U. Navi, B.A. Rosen, E. Sabatani, J. Tenenbaum, E. Tiferet, N. Eliaz, Thermal decomposition of titanium hydrides in electrochemically hydrogenated electron beam melting (EBM) and wrought Ti-6Al-4V alloys using in situ high-temperature X-Ray diffraction, Int J. Hydrog. Energy 46 (59) (2021) 30423–30432.
[27] J. Kim, E. Plancher, C.C. Tasan, Hydrogenation-induced lattice expansion and its effects on hydrogen diffusion and damage in Ti-6Al-4V, Acta Mater. 188 (2020) 686–696.
[28] N.U. Navi, J. Tenenbaum, E. Sabatani, G. Kimmel, R. Ben David, B.A. Rosen, Z. Barkay, V. Ezersky, E. Tiferet, Y.I. Ganor, N. Eliaz, Hydrogen effects on electrochemically charged additive manufactured by electron beam melting (EBM) and wrought Ti-6Al-4V alloys, Int J. Hydrog. Energy 45 (46) (2020) 25523–25540.
[29] E. Brosh, N.U. Navi, B.A. Rosen, N. Eliaz, Microvoids in electrochemically hydrogenated titanium-based alloys, Int J. Hydrog. Energy 46 (53) (2021) 27234–27242.
[30] S. Lynch, Hydrogen embrittlement phenomena and mechanisms, Corros. Rev. 30 (3–4) (2012) 105–123.

[31] A. Pundt, R. Kirchheim, Hydrogen in metals: microstructural aspects, Annu Rev. Mater. Res 36 (2006) 555–608.

[32] G.M. Pressouyre, Trap theory of hydrogen embrittlement, Acta Met. 28 (7) (1980) 895–911.

[33] S. Ifergane, Ben David, R. Sabatani, E. Carmeli, B. Beeri, O. Eliaz N, Hydrogen diffusivity and trapping in Custom 465® stainless steel, J. Electrochem Soc. 165 (3) (2018) C107–C115.

[34] N. Lulu-Bitton, E. Sabatani, B.A. Rosen, N. Kostirya, G. Agronov, E. Tiferet, N. Eliaz, N.U. Navi, Mechanical behavior of electrochemically hydrogenated electron beam melting (EBM) and wrought Ti-6Al-4V using small punch test, Int J. Hydrog. Energy 47 (9) (2022) 6388–6403.

[35] P. Metalnikov, D. Eliezer, G. Ben-Hamu, Hydrogen trapping in additive manufactured Ti-6Al-4V alloy, Mater. Sci. Eng. A 811 (2021) 141050.

[36] M. Neikter, M. Colliander, C.D. Schwerz, T. Hansson, P. Akerfeldt, R. Pederson, M. L. Antti, Fatigue crack growth of electron beam melted Ti-6Al-4V in high-pressure hydrogen, Materials 13 (6) (2020) 1287.

[37] S. Ifergane, E. Sabatani, B. Carmeli, Z. Barkay, V. Ezersky, O. Beeri, N. Eliaz, Hydrogen diffusivity measurement and microstructural characterization of Custom 465 stainless steel, Electro Acta 178 (2015) 494–503.

[38] T. Zakroczymski, Adaptation of the electrochemical permeation technique for studying entry, transport and trapping of hydrogen in metals, Electro Acta 51 (11) (2006) 2261–2266.

[39] M.A.V. Devanathan, Z. Stachurski, The adsorption and diffusion of electrolytic hydrogen in palladium, Proc. R. Soc. Lond. Ser. A 270 (1340) (1962) 90–102.

[40] ASTM G148-97, Standard practice for evaluation of hydrogen uptake, permeation, and transport in metals by an electrochemical technique. ASTM International, West Conshohocken, PA (2018) 2018.

[41] N. Eliaz, E. Gileadi, Physical. Electrochemistry: Fundamentals, Techniques, and Applications, second ed., Wiley-VCH, Weinheim, Germany, 2019, pp. 279–283.

[42] J. McBreen, L. Nanis, W. Beck, A method for determination of permeation rate of hydrogen through metal membranes, J. Electrochem Soc. 113 (11) (1966) 1218–1222.

[43] H.A. Estupiñan, I. Uribe, P.A. Sundaram, Hydrogen permeation in gamma titanium aluminides, Corros. Sci. 48 (12) (2006) 4216–4222.

[44] S. Huang, H.Y. Li, H. Zhang, J. Sheng, E. Agyenim-Boateng, J.Z. Lu, Experimental study and finite element simulation of hydrogen permeation resistance of Ti-6Al-4V alloy strengthened by laser peening, Surf. Coat. Technol. 400 (2020), 126217.

[45] Q. Zhang, Y. Huang, W. Sand, X. Wang, Effects of deep geological environments for nuclear waste disposal on the hydrogen entry into titanium, Int J. Hydrog. Energy 44 (23) (2019) 12200–12214.

[46] G.C. Yu, A comparison between proton and hydrogen chemical diffusion coefficients of titanium oxide films, Phys. Status Solidi a 198 (2) (2003), 302–11.

[47] V. Vij, S. Sultan, A.M. Harzandi, A. Meena, J.N. Tiwari, W.G. Lee, T. Yoon, K. S. Kim, Nickel-based electrocatalysts for energy-related applications: Oxygen reduction, oxygen evolution, and hydrogen evolution reactions, ACS Catal. 7 (10) (2017) 7196–7225.

[48] J. Cermak, A. Kufudakis, G. Gardavska, Diffusivity of hydrogen in platinum and the diffusion-elastic phenomenon. J. Less-Common Met. 63 (1) (1979) P1–P8.

[49] A. Turnbull, M. Saenz de Santa Maria, N.D. Thomas, The effect of H$_2$S concentration and pH on hydrogen permeation in AISI 410 stainless steel in 5% NaCl, Corros. Sci. 29 (1) (1989) 89–104.

[50] J. Crank. The Mathematics of Diffusion, second ed., Oxford University Press, London, UK, 1975.

[51] S. Hamada, K. Ohnishi, H. Nishikawa, Y. Oda, H. Noguchi, SIMS analysis of low content hydrogen in commercially pure titanium, J. Mater. Sci. 44 (20) (2009) 5692–5696.

[52] Z.H. Zhu, V. Shutthanandan, M. Engelhard, An investigation of hydrogen depth profiling using ToF-SIMS, Surf. Inter. Anal. 44 (2) (2012) 232–237.

[53] N. Mine, S. Portier, M. Martin, Imaging and hydrogen analysis by SIMS in zirconium alloy cladding: a dual ion beam approach, Surf. Inter. Anal. 46 (2014) 249–252.

[54] C.C. Hu, T.C. Wen, Voltammetric investigation of palladium oxides-I: their formation/reduction in NaOH, Electro Acta 40 (4) (1995) 495–503.

[55] Y. Zeng, J.J. Noël, P.R. Norton, D.W. Shoesmith, Hydrogen transport through thin titanium oxides, J. Electro Chem. 649 (1–2) (2010) 277–285.

[56] G.M. Pressouyre, I.M. Bernstein, A quantitative analysis of hydrogen trapping, Met. Trans. A 9 (11) (1978) 1571–1580.

[57] N. Pushilina, A. Panin, M. Syrtanov, E. Kashkarov, V. Kudiiarov, O. Perevalova, R. Laptev, A. Lider, A. Koptyug, Hydrogen-induced phase transformation and microstructure evolution for Ti-6Al-4V parts produced by electron beam melting, Metals 8 (5) (2018) 301.

[58] T. Zhu, M. Li, Effect of 0.770wt%H addition on the microstructure of Ti-6Al-4V alloy and mechanism of δ hydride formation, J. Alloy. Compd. 481 (2009) 480–485.

[59] C.C. Shen, C.M. Wang, Effects of hydrogen loading and type of titanium hydride on grain refinement and mechanical properties of Ti-6Al-4V, J. Alloy. Compd. 601 (2014) 274–279.

[60] M. Syrtanov, G. Garanin, E. Kashkarov, N. Pushilina, V. Kudiiarov, T. Murashkina, Laboratory X-ray diffraction complex for in situ investigations of structural phase evolution of materials under gaseous atmosphere, Metals 10 (4) (2020) 447.

[61] Y. Zhang, S.Q. Zhang, Hydrogenation characteristics of Ti-6Al-4V cast alloy and its microstructural modification by hydrogen treatment, Int J. Hydrog. Energy 22 (2–3) (1997) 161–168.

[62] Y. Liu, Z.H. Ren, J. Liu, R.F. Schaller, E. Asselin, Electrochemical investigation and identification of titanium hydrides formed in mixed chloride sulfuric acid solution, J. Electrochem Soc. 166 (11) (2019) C3096–C3105.

[63] M.N. Dogu, Z. Esen, K. Davut, E. Tan, B. Gumus, A.F. Dericioglu, Microstructural and texture evolution during thermo-hydrogen processing of Ti6Al4V alloys produced by electron beam melting, Mater. Charact. 168 (2020), 110549.

[64] E. Tal-Gutelmacher, D. Eliezer, The hydrogen embrittlement of titanium-based alloys, JOM 57 (9) (2005) 46–49.

[65] I. Paulin, D. Mandrino, C. Donik, M. Jenko, AES and XPS characterization of titanium hydride powder, Mater. Teh. 44 (2) (2010) 73–76.

[66] E. Kossoy, Y. Khoptiar, C. Cytermann, G. Shemesh, H. Katz, H. Sheinkopf, I. Cohen, N. Eliaz, The use of SIMS in quality control and failure analysis of electrodeposited items inspected for hydrogen effects, Corros. Sci. 50 (2008) 1481–1491.

[67] R. Ben David, Y. Finkelstein, E. Nativ-Roth, A. Danon, D. Cohen, E. Rabkin, The role of surface coarsening and sintering during thermal decomposition of titanium hydride, Int J. Hydrog. Energy 44 (12) (2019) 6045–6054.

[68] A.R. Gromov, N.N. Kouznetsova, S.L. Yudina, V.V. Lunin, The investigation of titanium hydride oxidation process, J. Alloy. Compd. 261 (1997) 269–272.

[69] V.A. Shutaev, E.A. Grebenshchikova, V.G. Sidorov, Yu.P. Yuakovlev, The influence of hydrogen on the optical transparency of palladium layers, Opt. Spectrosc. 128 (5) (2020) 596–599.

[70] K.J. Palm, J.B. Murray, T.C. Narayan, J.N. Munday, Dynamic optical properties of metal hydrides, ACS Photonics 5 (2018), 4677−86.

[71] R.J. Wasilewski, G.L. Kehl, Diffusion of hydrogen in titanium, Metallurgia 50 (1954) 225–230.

[72] B.G. Pound, Hydrogen ingress in titanium, Corrosion 47 (2) (1991) 99–104.